Application of Jetstream to a Suite of Aerodynamic Shape Optimization Problems

Karla Telidetzki,*

Lana Osusky † and David W. Zingg‡

Institute for Aerospace Studies, University of Toronto, Toronto, Ontario, M3H 5T6, Canada

This work demonstrates the performance of Jetstream, a high-fidelity aerodynamic shape optimization methodology for three-dimensional turbulent flows. The geometry parameterization and mesh movement is accomplished using B-spline volumes and linear elasticity mesh movement. The Euler or Reynolds-averaged Navier-Stokes (RANS) equations are solved at each iteration using a parallel Newton-Krylov-Schur method. The equations are discretized in space using summation-by-parts operators with simultaneous approximation terms to enforce boundary and block interface conditions. The gradients are evaluated using the discrete-adjoint method to allow for gradient-based optimization using a sequential quadratic programming algorithm. The goal of this work is to investigate the performance of Jetstream for three test problems. The first problem is the drag minimization of a two-dimensional symmetric airfoil in transonic inviscid flow, under a geometric constraint that the airfoil have a thickness greater than or equal to that of a NACA 0012 airfoil. Although the shock waves are not quite eliminated, they are substantially weakened, such that the drag coefficient is reduced by 86% compared to the NACA 0012 airfoil. The second problem is drag minimization through optimizing the twist distribution of a three-dimensional wing characterized by NACA 0012 sections in subsonic inviscid flow, subject to a lift constraint. A nearly elliptical spanwise lift distribution is achieved by the optimized twist distribution, leading to a span efficiency factor of 0.98. The third problem is drag minimization through optimizing the sections and twist distribution of the blunt-trailing-edge Common Research Model wing in transonic turbulent flow, subject to lift and pitching moment constraints. For this case the optimization is performed based on the solution of the RANS equations, with the Spalart-Allmaras turbulence model fully coupled and linearized. The drag coefficient is reduced by eleven counts, or 6%, when analyzed on a fairly fine mesh.

I. Introduction

Growth in air traffic is driving the need for more fuel efficient aircraft to reduce greenhouse gas emissions and fuel costs for airlines. Aerodynamic shape optimization has emerged in light of these issues. The use of aerodynamic shape optimization allows a computer algorithm to change the shape of an aerodynamic body such that it is optimal for a given set of conditions. This allows the human designer to focus on defining the priorities, objectives and constraints for the problem, rather than the aerodynamic shape. The goal is to optimize conventional geometries and to discover unconventional configurations.

Aerodynamic shape optimization involves four key steps: a geometry parametrization which defines the design variables that control the geometry change, movement of the computational grid with the geometry change, analysis of the flow, and an optimization algorithm. Each step influences the efficiency of the problem as well as the final solution. A number of different methods can be used at each step. For example, the geometry can be parameterized using a CAD package, basis splines, surface mesh nodes, or free form

*MASc Candidate

†PhD Candidate, AIAA Student Member

‡Professor and Director, Tier 1 Canada Research Chair in Computational Aerodynamics and Environmentally Friendly Aircraft Design, J. Armand Bombardier Foundation Chair in Aerospace Flight, Associate Fellow AIAA

deformation. The combination of all four steps produces an aerodynamic shape optimization algorithm through which airfoils, wings and complex blended wing body configurations can be optimized.

The computational fluid dynamics (CFD) community developed the drag prediction workshops in order to assess the performance of different CFD algorithms for aerodynamic flows. The aerodynamic optimization community lacks a similar suite of benchmark problems from which different algorithms can be compared. As a result, the community is holding a special session to assess and compare the different aerodynamic optimization algorithms on a suite of test problems and to further refine the test problems. The initial suite comprises four increasingly complex test cases. The first case is drag minimization of a two-dimensional NACA 0012 airfoil in transonic inviscid flow. The second is drag minimization of a two-dimensional RAE 2822 airfoil in transonic turbulent flow, subject to lift and pitching moment constraints. The third is drag minimization through optimizing the sections and twist distribution of a three-dimensional wing characterized by NACA 0012 sections in subsonic inviscid flow, subject to a lift constraint. The fourth is drag minimization through optimizing the sections and twist distribution of the blunt-trailing-edge Common Research Model (CRM) wing in transonic turbulent flow, subject to lift and pitching moment constraints.

This paper demonstrates the performance of Jetstream, a high-fidelity aerodynamic shape optimization algorithm for three-dimensional turbulent flows.[1,2,3] Three of the four benchmark cases are analyzed, with the two-dimensional RAE 2822 case omitted. For each case, a systematic study is performed on the impact of the number of design variables. The objective of this study is to provide guidance on how to best parametrize the geometry and set up the optimization problem for the benchmark cases, and to characterize the performance of the various components of Jetstream

II. Geometry Parameterization and Mesh Movement

Several different geometry parameterization techniques have been used for aerodynamic shape optimization, each having their advantages and disadvantages. A good parameterization should be able to approximate a wide variety of aerodynamic shapes while using as few design variables as possible. The parameterization in the present algorithm uses B-spline tensor volumes to approximate not only the surface, but the entire multi-block structured computational mesh, and was developed by Hicken and Zingg.[3] As a result, the geometry parameterization is integrated with the mesh movement scheme. This section provides a brief outline as to how B-spline volumes are utilized to create a fitted control mesh, and how this control mesh is integrated into the mesh movement scheme.

A. B-Spline Volumes

The computational mesh is controlled using a control mesh composed of B-spline volumes. This control mesh is several orders of magnitude smaller than the computational mesh. The coordinates of the mesh nodes $\mathbf{X}$ are found as a function of the parametric space $\boldsymbol{\xi}$ through

$$\mathbf{X}(\boldsymbol{\xi}) = \sum_{i=1}^{N_i}\sum_{j=1}^{N_j}\sum_{j=1}^{N_k} \mathbf{B}_{ijk}\mathcal{N}_i(\xi)\mathcal{N}_j(\eta)\mathcal{N}_k(\zeta), \tag{1}$$

where $\boldsymbol{\xi} = (\xi, \eta, \zeta)$, and $\mathbf{B}_{ijk}$ represents the set of points that define the control mesh. The basis functions are $\mathcal{N}_i(\xi)$, $\mathcal{N}_j(\eta)$ and $\mathcal{N}_k(\zeta)$. These basis functions are a modified version of the standard B-spline basis, differing through the use of spatially varying knot vectors. The control points of the B-spline patches that represent the aerodynamic surface serve as design variables controlled by the optimization algorithm.

B. Linear Elasticity Mesh Movement

In order for aerodynamic shape optimization to occur, geometry changes must be accommodated by both the parameterization and the mesh movement schemes. By fitting the computational mesh with B-spline volumes, changes in the design variables, i.e. the control points on the B-spline surface, can be propagated through the mesh using a method based on the principles of linear elasticity, which was adapted from the work of Truong et al.[4] by Hicken and Zingg.[3] Using a method based on linear elasticity is generally computationally expensive; however, the control mesh made up of the B-spline volume control points is typically two orders of magnitude smaller than the full computational mesh, reducing the computational time substantially.

The volumes of the control mesh are treated as linear elastic solids that are isotropic and homogeneous. A linear relationship between the stress tensor and Cauchy stress tensor is assumed, with a Poisson's ratio of $\nu = -0.2$ used in this work to keep the cell aspect ratios from becoming too large. To accommodate large shape changes and improve robustness, the mesh movement occurs in increments. This work uses $m = 5$ increments, but if mesh movement problems occur, it is possible to use more increments. The coordinates of the intermediate surface control points are related to their initial $b_s^{(0)}$ and final $b_s^{(m)}$ values using a linear relationship

$$b_s^{(i)} = \frac{i}{m}(b_s^{(m)} - b_s^{(0)}) + b_s^{(0)}, \quad i = 1, ..., m. \tag{2}$$

The equation of linear elasticity is discretized on the control mesh using a finite-element method. The resulting linear system is solved using the conjugate gradient method preconditioned with ILU(1),[5] with the convergence criterion being a reduction in the L_2 norm to a relative tolerance of 10^{-12}. The fine mesh is then updated from the control mesh using an algebraic approach based on the B-spline volume basis functions.

III. Flow Solver

The flow solver is one of the key components of any aerodynamic shape optimization algorithm. The flow solver should be efficient, accurate and robust. Accuracy is required to allow the optimizer to use the information from the flow solver to produce an optimum solution. Efficiency is required as the optimizer will perform many flow solves through the course of an optimization. Robustness is necessary to accommodate significant geometry changes. This section presents a brief description of the parallel three-dimensional multi-block structured solver.

The parallel implicit flow solver uses a Newton-Krylov-Schur method to obtain flow solutions for use within the aerodynamic shape optimization algorithm. The flow solver was developed by Hicken and Zingg[6] for the three-dimensional Euler equations, and by Osusky and Zingg[7] for the three-dimensional Reynolds-averaged Navier-Stokes (RANS) equations. The RANS equations are fully coupled with the Spalart-Allmaras one-equation turbulence model. The governing equations are discretized using second-order Summation-by-Parts (SBP) operators. Boundary and block interface conditions are enforced weakly through Simultaneous Approximation Terms (SATs). The Newton method produces a large, sparse system of linear equations that is solved using flexible GMRES (FGMRES) with an approximate-Schur parallel preconditioner. An approximate Newton start-up phase is used to provide the initial iterate for the inexact-Newton phase.

IV. Optimization Algorithm

The optimization algorithm used, SNOPT (Sparse Nonlinear OPTimizer), was developed by Gill, Murray and Saunders.[8] It is a gradient-based optimizer capable of finding a local optimum for a constrained optimization problem. It is capable of handling both linear and nonlinear constraints, with the linear constraints being satisfied exactly. For a typical aerodynamic shape optimization problem, the objective function is nonlinear, and the constraints imposed are a combination of linear and nonlinear constraints. For this type of problem, SNOPT applies a sparse sequential quadratic programming (SQP) method that uses a limited-memory quasi-Newton approximation to the Hessian.

On large problems, SNOPT performs most efficiently if only some of the variables are nonlinear or if there are relatively few degrees of freedom at a solution (meaning many of the inequality constraints are at their bounds). For an aerodynamic shape optimization problem, where the lift and drag coefficients depend on the geometry, all the design variables will enter the problem nonlinearly. As the number of design variables increases, the convergence of the optimizer will be affected. In addition, the presence of more design variables can produce geometries that do not allow convergence of the mesh movement algorithm or the flow solver. When either of these situations occur, SNOPT must find a way back into a region with defined functions by shortening the step length it takes along the search direction. If it is not able to get back into a region with defined functions using this method, the algorithm will terminate. It is therefore reasonable to expect that the number of control points used to parameterize the geometry could impact the convergence of SNOPT. The convergence histories that will be presented in this paper use an optimality measure that is closely related to the KKT conditions.

A. Gradient Evaluation

To use a gradient-based optimization method, the gradient must be computed accurately and efficiently. Using finite differencing is not possible for the problems in question, as there are too many design variables, and it would be prohibitively inefficient. Pironneau[9] and Jameson[10] proposed the adjoint method, which allows the gradient to be computed at a cost that is virtually independent of the number of design variables. This work uses the discrete adjoint method, rather than the continuous form. The mesh movement and flow residual equations are treated as nonlinear constraints that are solved outside of SNOPT. For the objective function and each flow constraint (e.g. a lift constraint), an adjoint problem is solved for the flow residual and mesh movement increment. The flow Jacobian matrix is formed by linearizing its components, including the viscous and inviscid fluxes, the numerical dissipation, the turbulence model, and the boundary conditions. This linearization was completed by Hicken and Zingg[6] and Osusky and Zingg.[1] The size of the mesh adjoint equations is proportional to the number of nodes in the control mesh; hence these are inexpensive to solve. A preconditioned conjugate-gradient method is used to solve the system to a tolerance of 1×10^{-12}. The flow adjoint system is solved using a modified, flexible version of GCROT developed by Hicken and Zingg,[11] found to be more effective than GMRES when deep convergence is needed, to a tolerance of 1×10^{-10}.

V. Results

This section presents the performance of Jetstream on three benchmark aerodynamic optimization problems. For all of the cases the impact of dimensionality is investigated by varying the number of control points parameterizing the surface and hence varying the number of design variables.

A. Case 1: Symmetrical Airfoil Optimization in Transonic Inviscid Flow

This case involves drag minimization of the NACA 0012 airfoil in transonic, inviscid flow based on Vassberg et al.[12] The number of control points used to parameterize the airfoil is varied to investigate the effect the parameterization has on the optimization. In a two-dimensional inviscid flow, the only source of drag, other than numerical error (including the effect of the finite distance to the far-field boundary), is wave drag. Hence if the shocks can be eliminated, the drag is strictly a consequence of numerical error.

Optimization Problem

The optimization problem can be summarized as

$$\begin{aligned} &\text{minimize } C_{\mathrm{D}} \\ &\text{subject to } z \geq z_{\text{baseline}} \end{aligned}$$

where C_{D} is the drag coefficient, z is the vertical coordinate of the optimized geometry, and z_{baseline} is the vertical coordinate of the baseline geometry. The geometry is subject to a minimum thickness constraint which requires the optimized geometry to be greater in thickness than the baseline geometry. This thickness constraint is enforced by constraining each control point such that it may only move outside its original location. Since the initial airfoil is symmetric, the resulting lift coefficient is zero, which should be maintained throughout the optimization. The symmetry is enforced by adding linear constraints to the control points on the upper and lower surfaces that force them to be equal and opposite in sign. The optimization is given an optimality tolerance of 10^{-7}; however not all cases are able to achieve this level of convergence. The feasibility tolerance does not affect this optimization, as there are no nonlinear constraints.

Flow Conditions

The flow is inviscid and transonic with a freestream Mach number of $M = 0.85$ and zero angle of attack ($\alpha = 0°$).

Baseline Geometry

The NACA 0012 airfoil is modified to have a zero thickness trailing edge. The modified airfoil is defined as

$$z_{\text{baseline}} = \pm 0.6(0.2969\sqrt{x} - 0.1260x - 0.3516x^2 + 0.2843x^3 - 0.1036x^4), \quad x \in [0, 1], \tag{3}$$

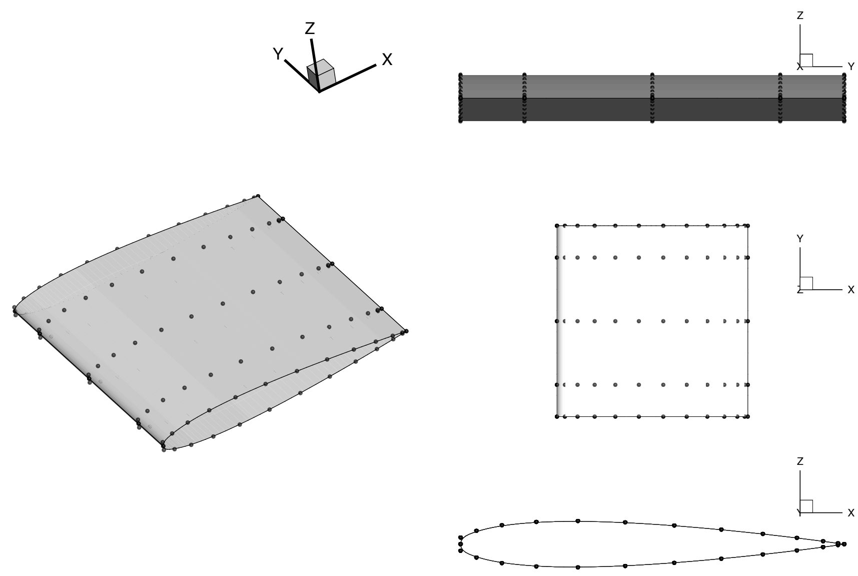

Figure 1. NACA0012 initial geometry

where the modification to the trailing edge occurs via a change in the x^4 term. In order to use the three-dimensional optimization algorithm, the optimization is performed using an extruded airfoil. The airfoil is extruded one chord length, so it has a chord of one unit and a span of one unit. The extruded airfoil is composed of an upper and lower patch. Each patch is parameterized using a variable number of control points in the streamwise direction and a constant number of control points (five) in the spanwise direction. Figure 1 shows the initial geometry parameterized with fourteen streamwise control points on each surface.

The initial geometry is created by fitting a B-spline curve through NACA 0012 data points obtained from an input data file, with z-coordinates Z_S. In order to fit a given curve using a B-spline curve, the given curve must be parameterized, with a chord length parameterization used in Jetstream. The residual of the fit can be calculated by comparing the z-coordinates of the B-spline curve, Z_B, to the initial NACA 0012 z-coordinates:

$$\|Z_S - Z_B\|_2 \, , \tag{4}$$

A better fit can be obtained by changing the values of the parameters through an iterative parameter correction procedure, such as that suggested by Hoschek.[13] Figure 2 shows that the residual of the initial fit without parameter correction can be quite poor, depending on the number of streamwise control points used. Introduction of the parameter correction has a large impact on the fit, especially for a small number of control points.

Grid

A structured grid is created around a flat plate with a chord length of one unit and a span of one unit. The mesh movement capabilities of the algorithm are then used to inflate this flat plate into an extruded airfoil with the sections determined from the B-spline fit of the NACA 0012 airfoil. Just as the geometry can be thought of as the extrusion of a two-dimensional airfoil, the grid can be thought of as an extrusion of a two-dimensional grid. There are ten nodes in the extruded direction, meaning the three-dimensional grid is ten times larger than its equivalent two-dimensional grid. Four different grid levels were created by starting with a fine grid and removing every other grid node, except in the extruded direction where the number of nodes remains constant. Figure 3 shows the coarse grid level.

Table 1 outlines the number of nodes, streamwise spacing at leading and trailing edges, and off-wall spacing of the different grid levels. The number of nodes reported is the two-dimensional equivalent, calculated by taking the total number of nodes in the three-dimensional grid and dividing by ten (the number

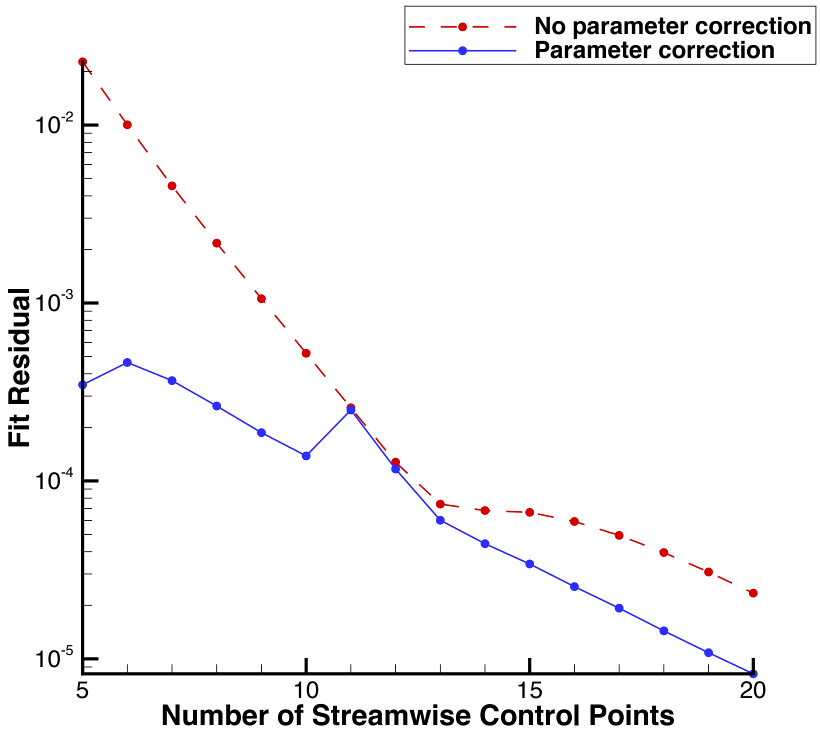

Figure 2. Effect of parameter correction

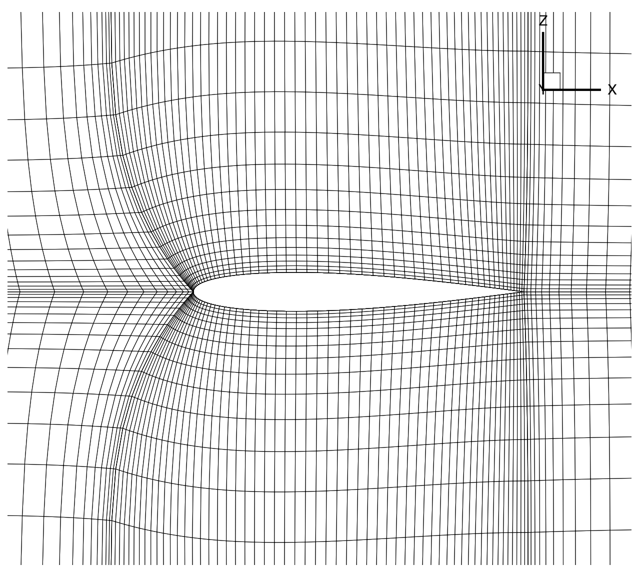

Figure 3. Coarse grid level

of nodes in the extruded direction). A grid convergence study was conducted by first performing a flow solve on each grid level. The geometry is parameterized using five streamwise control points. Table 2 shows that when performing a flow solve on the three finest grid levels, the drag is increasing monotonically as the grid is refined. The order of accuracy is calculated to be $p = 1.61$, and the grid converged value of drag is $C_D^* = 4.2611883 \times 10^{-2}$. The order of accuracy compares well to the expected order of 2. A complete optimization was then performed on each grid level with three design variables (the leading and trailing

Table 1. Grid convergence study data (all spacings in chord units)

Grid	Nodes (2D Equivalent)	Off-wall Spacing	Leading-Edge Spacing	Trailing-Edge Spacing
Coarsest	3450	0.016	0.016	0.016
Coarse	12760	0.008	0.008	0.008
Medium	49020	0.004	0.004	0.004
Fine	192100	0.002	0.002	0.002

Table 2. Flow solve only

Grid Level	Nodes (2D Equivalent)	Lift Coefficient, C_{L}	Drag Coefficient, C_{D}
Coarsest	3450	-3.0559469E-008	4.4009627E-002
Coarse	12760	-3.2604330E-008	4.2368198E-002
Medium	49020	-3.7684892E-008	4.2412170E-002
Fine	192100	-3.4642657E-008	4.2546515E-002

Table 3. Final optimized geometry with flow solve analysis on finest grid level

Grid Level	Nodes (2D Equivalent)	Lift Coefficient, C_{L}	Drag Coefficient, C_{D}
Coarsest	3450	1.8393958E-008	3.8512258E-002
Coarse	12760	-5.0866142E-009	3.8512774E-002
Medium	49020	-6.7404717E-009	3.8512141E-002
Fine	192100	4.8072657E-013	3.8511493E-002

edge control points are fixed), and a flow solve performed on each optimized geometry using the fine grid level. Table 3 shows that when performing the optimization all four grid levels, even the coarsest, produce geometries with very similar drag coefficients. The drag coefficients of the optimized geometries, solved on the fine grid level, are all within 0.01 of a drag count of each other. The lift coefficients are all effectively zero. The results of this study show that it is possible to perform optimization on the coarse grid level to conserve computational time, and analyze the final geometry with the fine grid level. This is the method employed for the results to follow.

Optimization Results

The results obtained using Jetstream are compared to the Phase I and Phase III results obtained by Vassberg et al. in Figure 4. The number of design variables (DVs) is varied from 3 to 16. The leading edge and trailing edge control points are fixed in all cases. All cases are optimized on the coarse grid used in the grid convergence study, with a flow solve performed on the final geometries using the fine grid. All functionals shown are those computed on the fine grid. As shown in Figure 5, the optimization convergence of the cases degrades as the number of design variables is increased. For up to 12 design variables a two order of magnitude reduction in optimality is achieved.

The lowest drag coefficient is obtained with 8 design variables: 60.8 drag counts, which is a reduction of 86% relative to the baseline geometry. Figure 6 shows the airfoil shapes obtained by Jetstream for three different parameterizations. As the number of control points is increased, the airfoil becomes thicker near the trailing edge. Figure 7 shows the surface pressure coefficient distributions. The shock is pushed further downstream, close to the trailing edge. Figures 8 and 9 show the Mach and entropy contours for the 6 DV and 12 DV optimized airfoils. Although the shock is not completely eliminated, it extends only a very small distance into the flow. Future work should concentrate on obtaining optimization convergence with more design variables to see if further drag reduction can be achieved. However, it should be noted that this is largely a testing exercise, as the resulting airfoil is likely to be of little practical use, since the adverse pressure gradient near the trailing edge will lead to boundary-layer separation.

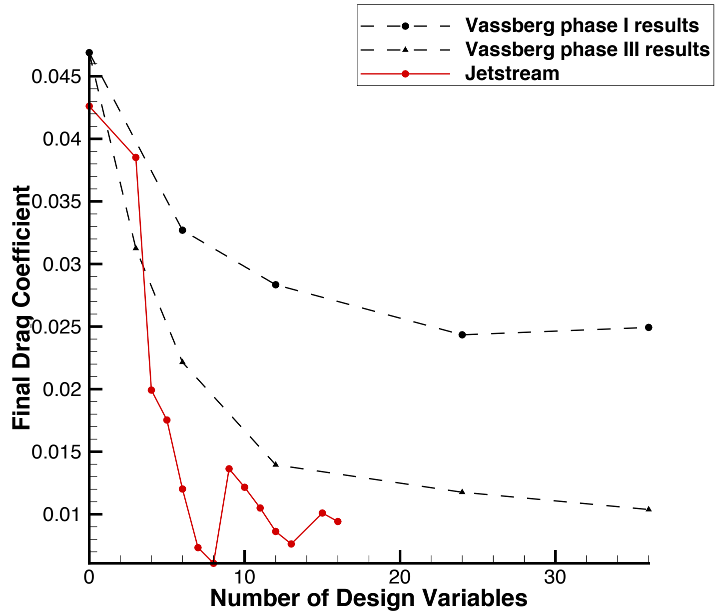

Figure 4. Comparison of symmetric airfoil results with Vassberg et al. results[12]

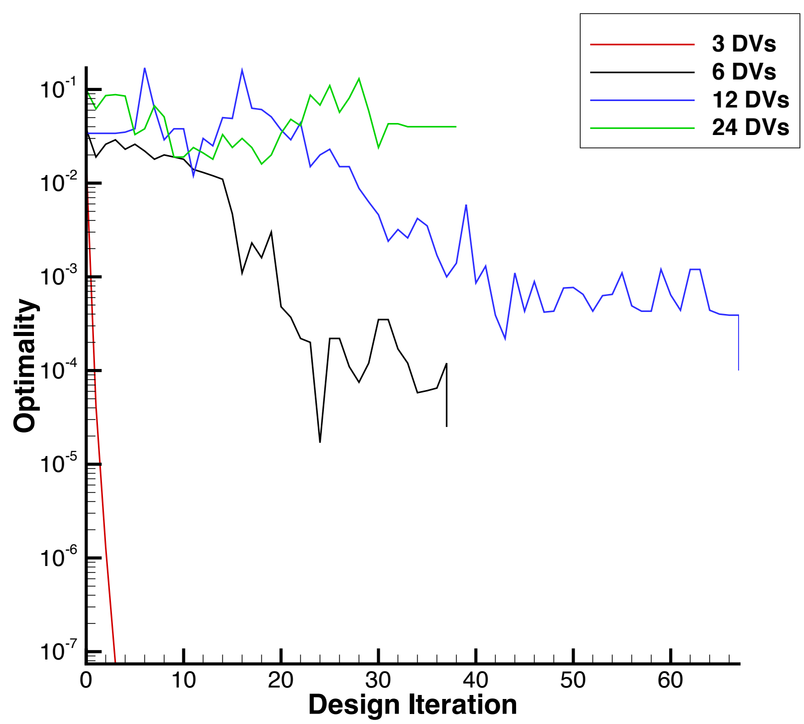

Figure 5. Typical optimization convergence histories for NACA 0012 airfoil case

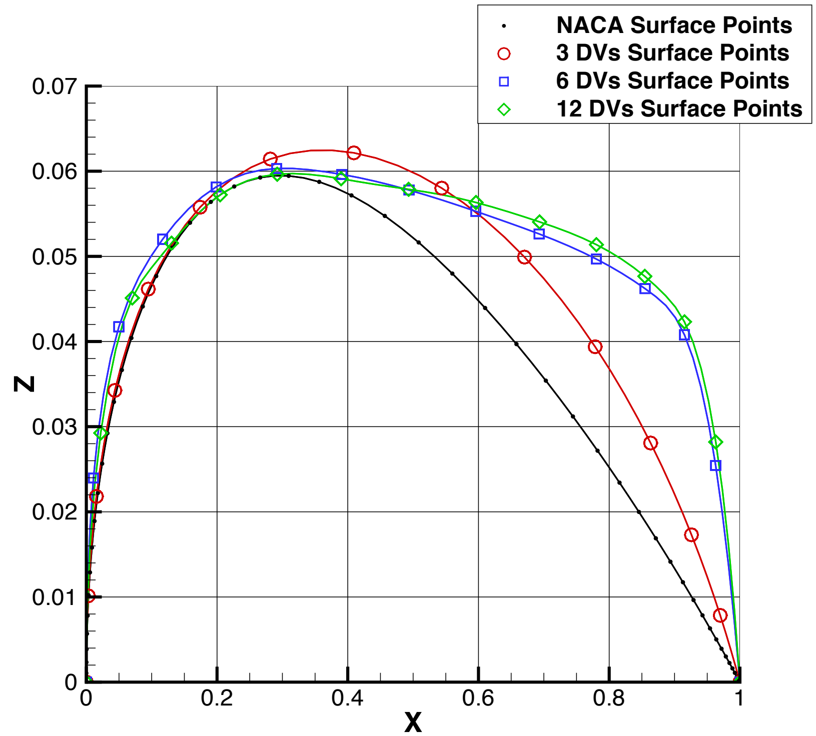

Figure 6. Airfoil shapes

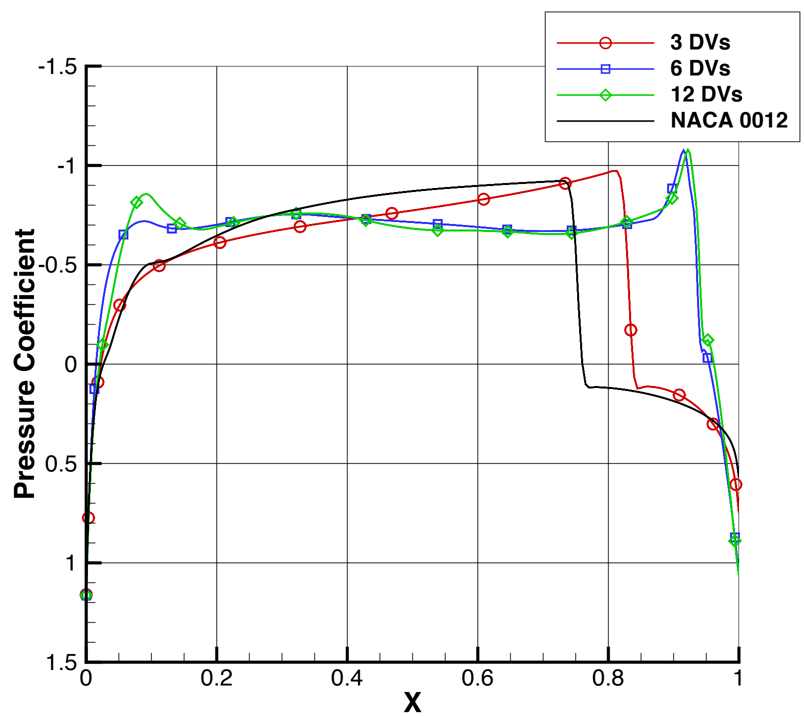

Figure 7. Coefficient of pressure distrbutions

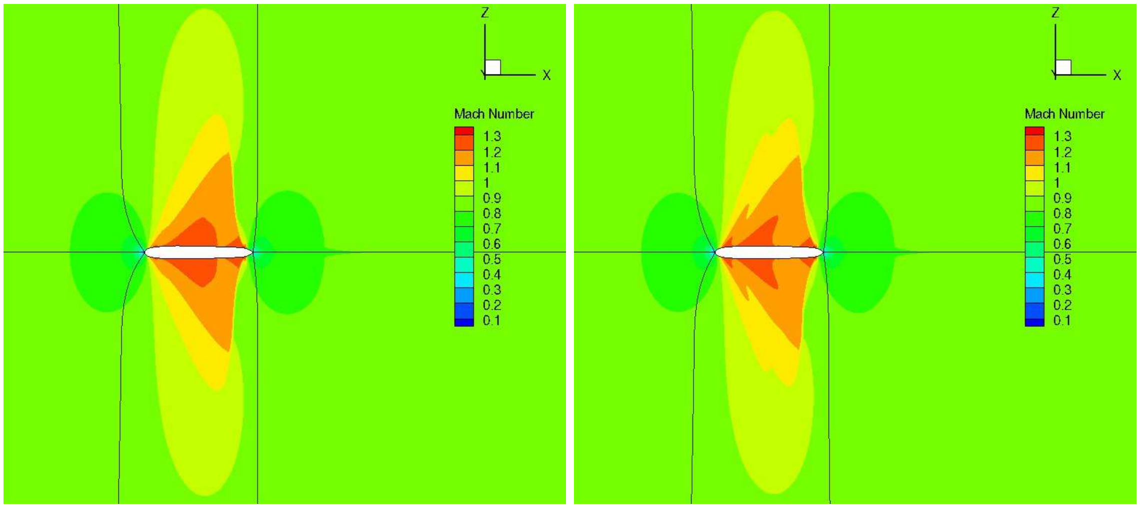

(a) 6 DVs (b) 12 DVs

Figure 8. Mach contours

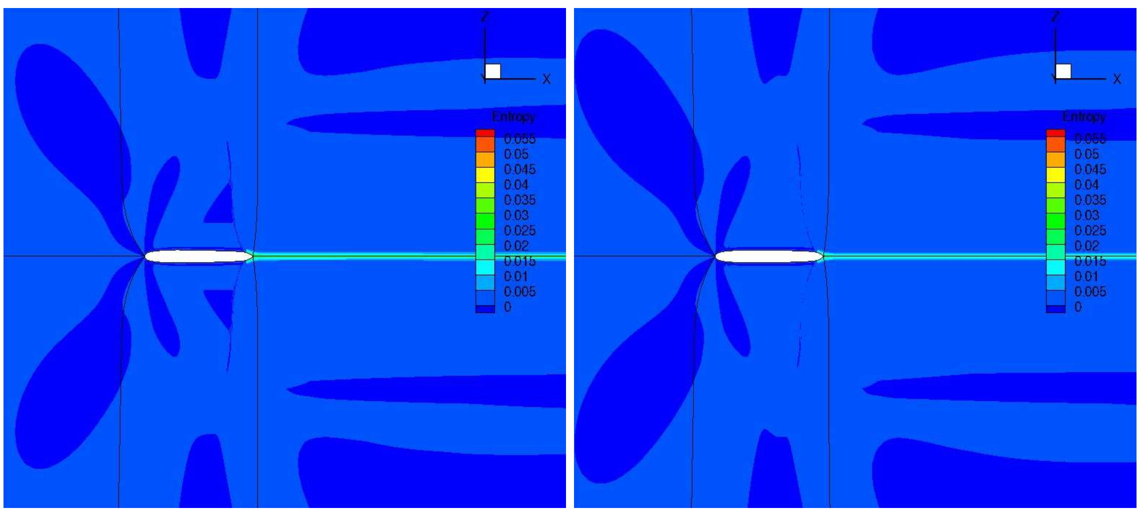

(a) 6 DVs (b) 12 DVs

Figure 9. Entropy contours

B. Case 2: Twist Optimization of a Rectangular Wing in Subsonic Inviscid Flow

The second case investigated in this paper is the drag minimization of a rectangular wing with NACA 0012 sections through optimization of the twist distribution about the trailing edge. The number of design variables is varied to investigate the effect on the optimization. The flow is subsonic and inviscid, hence the goal is to minimize the induced drag at a fixed lift coefficient. The optimization should recover a lift distribution that is close to elliptical and a span efficiency factor close to one. The span efficiency factor is calculated using

$$e = \frac{C_{\mathrm{L}}^2}{\pi \Lambda C_{\mathrm{D_i}}} \tag{5}$$

where e is the span efficiency factor, C_{L} is the lift coefficient, Λ is the aspect ratio and $C_{\mathrm{D_i}}$ is the induced drag coefficient.

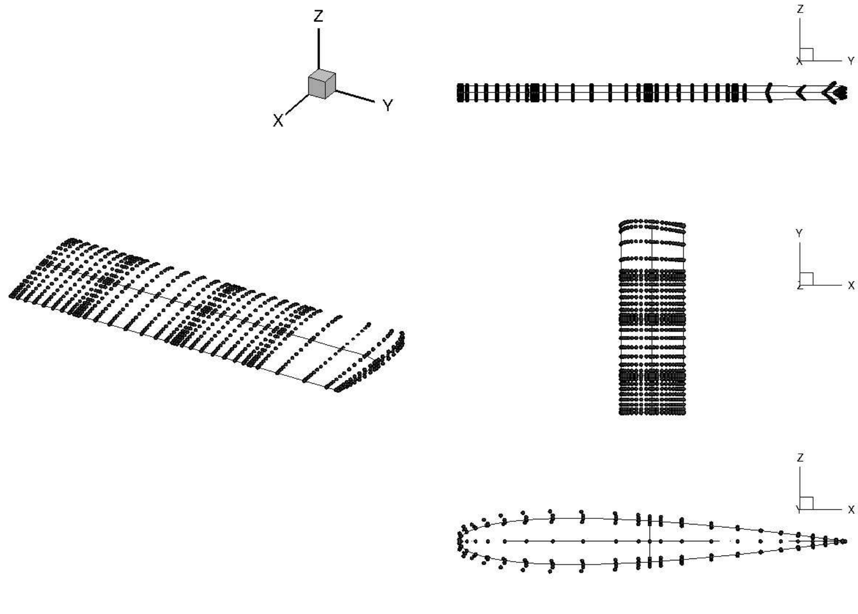

Figure 10. NACA 0012 rectangular wing initial geometry

Optimization Problem

The optimization problem is formally described as

$$\text{minimize } C_{\mathrm{D}}$$
$$\text{subject to } C_{\mathrm{L}} = 0.375$$

where C_{D} is the drag coefficient and C_{L} is the lift coefficient. The wing is twisted about the trailing edge at a finite number of stations through the use of linear constraints. This is accomplished by varying the z coordinates, so the projected surface area remains constant. The span and aspect ratio are also fixed, so the only mechanism to reduce the induced drag coefficient is through the span efficiency factor, which is related to the spanwise load distribution. The tip is constrained to be a linear shear of the twist of the last two spanwise stations. This prevents the optimizer from twisting the tip so drastically that it creates a winglet. The lift constraint is the only nonlinear constraint implemented. The angle of attack is a design variable, and the root section is fixed. The optimization is given an optimality tolerance of 10^{-6}; however, as in the first case, not all cases are able to achieve this level of convergence. The feasibility tolerance is 10^{-6}, which defines the tolerance to which the nonlinear lift constraint must be satisfied.

Flow Conditions

The flow is invisicid and subsonic. The freestream Mach number is $M = 0.5$, and the initial angle of attack is $\alpha = 4.4°$.

Baseline Geometry

The geometry is a rectangular wing with NACA0012 sections which have been modified to have a sharp trailing edge (see Equation 3). The wing has a semispan of 3.06 chords, consisting of 3 chords of rectangular planform and 0.06 chords of wing-tip cap. The geometry has sixteen surface patches, twelve inboard (upper and lower) that have a variable spanwise parameterization and four outboard (upper and lower) that have a constant spanwise parameterization to ensure a consistent tip geometry. Figure 10 shows the geometry with 13 streamwise and 11 spanwise control points on each inboard patch.

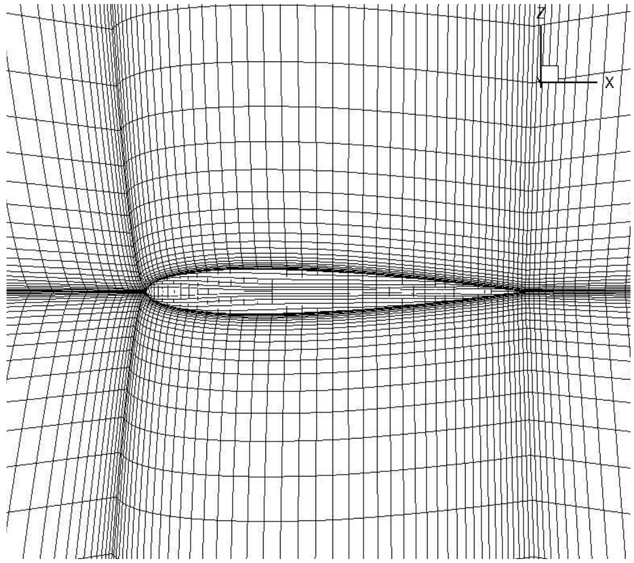

Figure 11. Grid at wing root

Grid

The grid has approximately 1.4 million nodes. The off-wall spacing is 0.002 chords, the streamwise leading-edge spacing is 0.005 chords, and the streamwise trailing-edge spacing is 0.01 chords. Figure 11 shows a close-up of the node distribution around the grid at the root.

Optimization Results

The number of control points is varied from 5 to 11 in the spanwise direction, with 13 control points used in the streamwise direction on each patch. Figure 12 shows the final drag coefficients for a number of different parameterizations. All of the cases are able to achieve the required optimality tolerance. Figure 13 shows two optimization convergence histories.

Figure 14, plots the initial and final span efficiency factors. The initial span efficiency factor is just below 0.962, and the final span efficiency factor varies from 0.979 to 0.98. These are likely not grid converged and will increase if computed on a finer mesh. Hence these can be thought of as relative values and it is more instructive to look at Figure 15, which shows the overall change in efficiency from the initial to the optimized shape. As the number of spanwise control points increases, the optimizer is able to produce a slightly greater improvement in efficiency. Figure 16 shows the spanwise lift distribution for the case with 11 spanwise control points per patch, which is very close to elliptical.

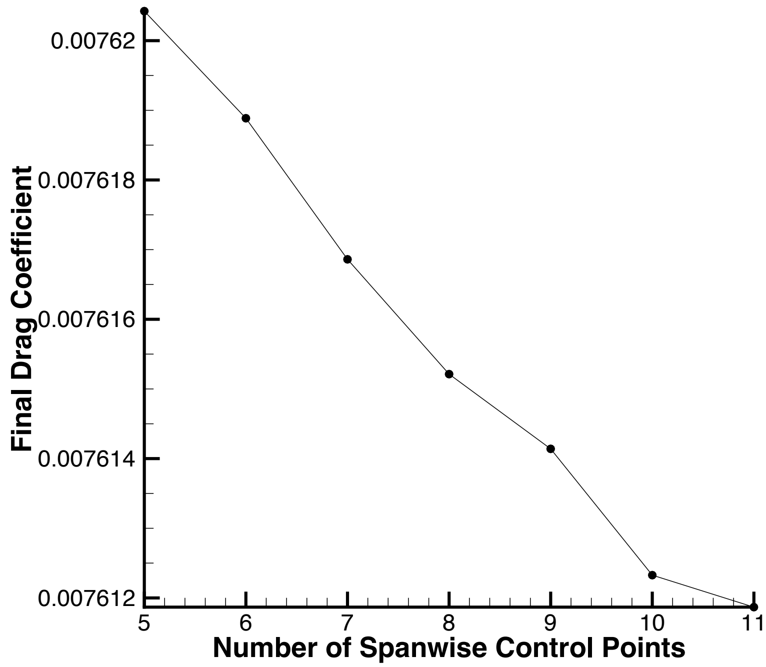

Figure 12. Final drag coefficient for NACA 0012 wing twist case

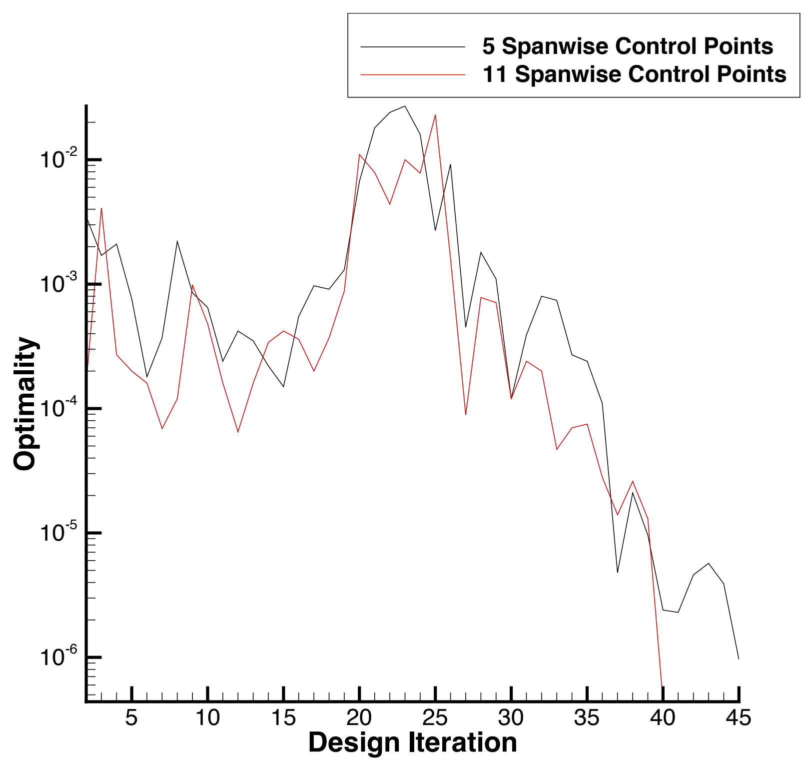

Figure 13. Sample convergence histories for NACA 0012 wing twist case

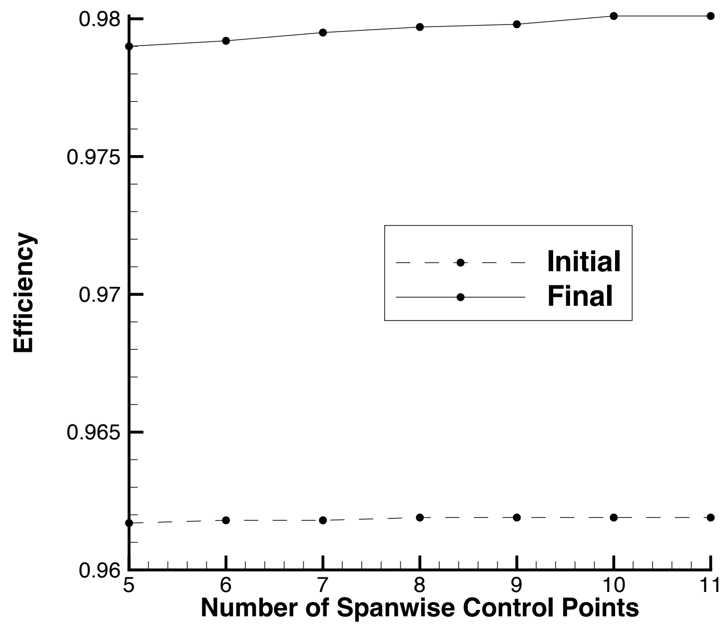

Figure 14. Initial and final span efficiencies for NACA 0012 wing twist case

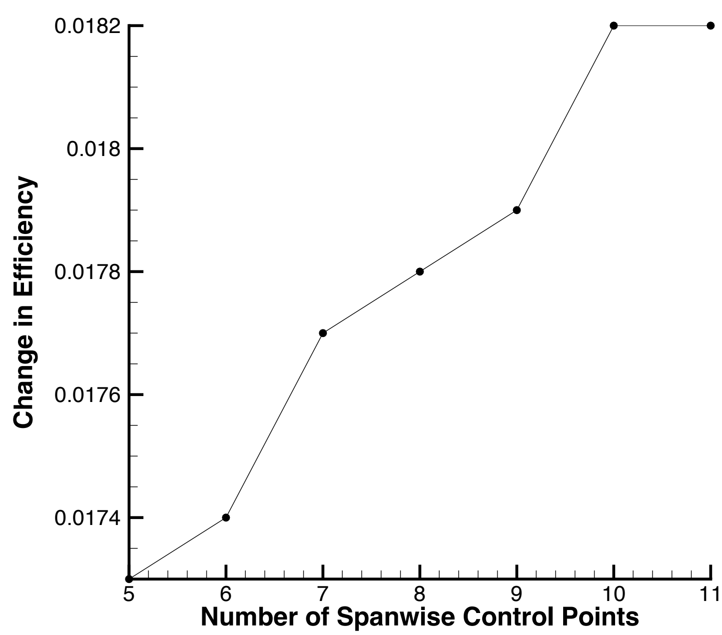

Figure 15. Change in span efficiency for NACA 0012 wing twist case

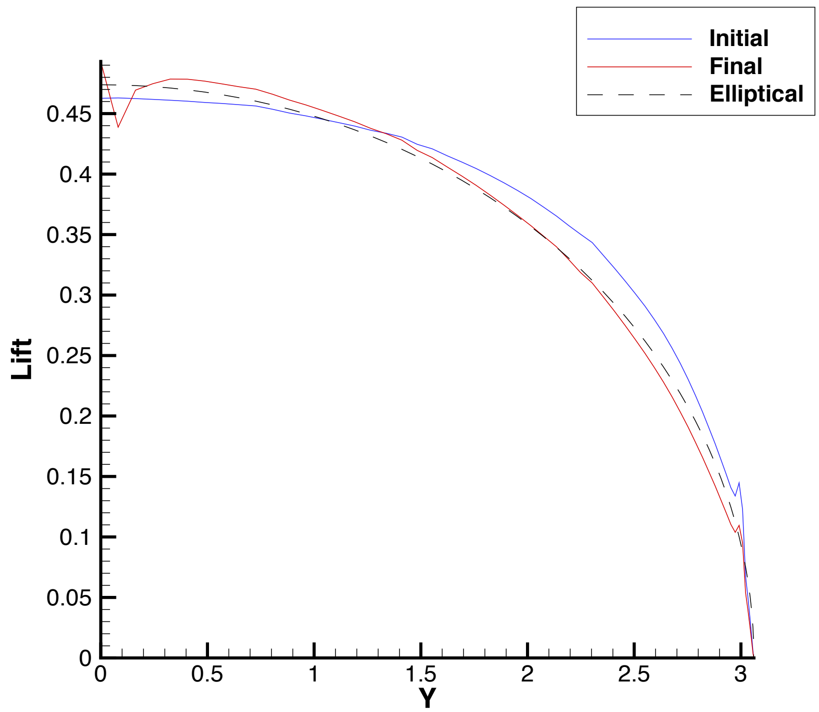

Figure 16. Spanwise lift distribution with 11 spanwise control points per patch

C. Case 3: Wing Twist and Section Optimization in Transonic Turbulent Flow

The final case is the lift-constrained drag minimization of the Common Research Model (CRM) wing-only geometry in fully turbulent transonic flow. The z-coordinates of the control points are design variables, allowing for both twist and section shape optimization. Since this flow is viscous and transonic all three types of drag are captured by the flow solver, viscous drag, lift-induced drag and wave drag.

Optimization Problem

The optimization problem is

$$\begin{aligned} \text{minimize } & C_{\mathrm{D}} \\ \text{subject to } & C_{\mathrm{L}} = 0.5 \\ & C_{\mathrm{M}} \geq -0.17 \end{aligned}$$

where C_{D} is the drag coefficient, C_{L} is the lift coefficient, and C_{M} is the pitching moment coefficient. The initial planform area, which is fixed throughout the optimization, is 3.407014 squared reference units. Both section changes and twist are permitted. This is achieved by allowing control point movement in the vertical (z) direction and fixing the trailing edge. The planform area is fixed, and the angle of attack is a design variable. The lift coefficient is constrained at $C_{\mathrm{L}} = 0.5$, and the pitching moment coefficient is constrained at $C_{\mathrm{M}} \geq -0.17$. There is a volume constraint such that the total wing volume is greater than or equal to its initial value. The thickness of the sections must be greater than or equal to 25% of the initial thickness.

Flow Conditions

The flow is viscous, transonic, and fully turbulent. The Mach number is 0.85, Reynolds number 5 million, and the initial angle of attack 2.2 degrees. The pitching moment is taken about the point (1.2077, 0, 0.00769).

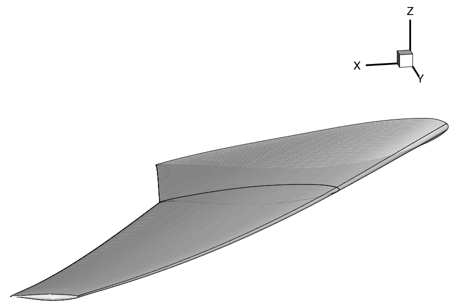

Figure 17. Initial CRM wing geometry

Baseline Geometry

The baseline geometry is the extracted wing from the Common Research Model, which was used in the Fourth and Fifth Drag Prediction Workshops.[14,15] The geometry, shown in Figure 17, features a blunt trailing edge. The wing geometry is extracted by deleting the fuselage from the wing-body geometry, leaving the wing root located at a distance of 120.52 inches from the original symmetry plane. The leading edge of the wing root is translated to the origin, and all grid coordinates are scaled by the mean aerodynamic chord (MAC) of 275.8 inches. A post-processing script is applied to all nodes on the symmetry plane to ensure that they are at $y = 0$.

Grid

An O-O topology computational mesh made up of 18 blocks and 3.38 million nodes is used for the parameterization of the geometry. Flow analysis is performed on a mesh that is created by subdividing each block of the parameterization mesh into 8 sub-blocks, resulting in a 144-block, 3.57 million-node mesh, enabling perfect load balancing on 144 processors. The MAC is used as the reference length. The mesh has an off-wall spacing of 2.56×10^{-6} reference units, resulting in an average y^+ value of 1.0. The wing geometry has 9 surface patches: 2 each on the upper and lower surfaces, 2 each along the leading edge and blunt trailing edge, and one cap patch at the wing tip. The leading-edge patches (one for the inboard section and one for the outboard) are required in order to match with the blunt trailing-edge patches, and also serve as a method of better capturing the curvature of the leading edge.

Optimization is performed for a geometry where each surface patch is parameterized with 7 control points in the streamwise direction and 5 in the spanwise direction, with the exception of the patches along the leading and trailing edges, which have 5 control points in the streamwise direction. The control points at the trailing edge are fixed, as is the control point at the leading-edge of the root section, while the remaining control points are allowed to move vertically. Along with the angle of attack, this results in 150 design variables.

To ensure that the improvement in the drag coefficient carries over to finer grid levels, the initial and optimized geometries are analyzed on a finer mesh made up of 39.4×10^6 nodes. The lift, drag, and pitching moment coefficients obtained on the fine mesh are compared to those obtained on the 3.6×10^6-node mesh used in the optimization in Table 4. Neither the pitching moment coefficient nor the drag coefficient are grid converged. The pitching moment constraint is enforced on the coarser mesh and thus is violated when the analysis is performed on the finer mesh. However, the difference is less than 2%. The drag coefficients computed on the finer mesh are 4-7% lower than those computed on the coarser mesh. When analyzed on the finer mesh, the drag reduction achieved by the optimized geometry relative to the initial geometry is 11 counts, or 6%.

Table 4. Coefficients for CRM wing with blunt trailing edge on optimization mesh and fine mesh

	Initial Geometry		Optimized Geometry	
Mesh Size (nodes)	3.6×10^6	39.8×10^6	3.6×10^6	39.8×10^6
C_L	0.500	0.500	0.500	0.500
C_D	0.0212	0.0197	0.0193	0.0186
C_M	-0.1740	-0.1862	-0.1700	-0.1730

Optimization Results

Figure 18 shows two sample optimization convergence histories. The optimality measure is reduced by only roughly an order of magnitude. It is possible that deeper convergence can be achieved if geometric constraints are added to limit deformations near the leading and trailing edges and the wing tip. Figure 19 shows the dependence of the drag coefficient computed for the optimized geometries on the number of spanwise control points, showing a slight reduction as the number of spanwise control points is increased.

The spanwise lift distribution for the optimized geometry with 7 spanwise control points is plotted in Figure 20, showing that the optimizer has made the distribution more elliptical and hence reduced induced drag. Surface pressure coefficient distributions and section shapes are displayed in Figures 21 and 22, respectively. The pressure distributions show that the optimizer has modified the geometry to weaken or eliminate shock waves, thereby reducing wave drag. Toward the wing tip, the optimized geometry displays a rather pointed leading edge, which may be undesirable structurally and when the wing is operated at lower angles of attack. This feature is easily avoided either through geometric constraints, or more preferably through multipoint optimization.[16] Similarly, the trailing edge shape seen, for example, at 55.7% span may be inadequate structurally. This can also be avoided either through geometric constraints or aerostructural optimization. We emphasize that the purpose of this test case is to characterize the performance of the optimization methodology; this is not a practical design example, which would require many more considerations.

VI. Conclusions

This paper has investigated the performance of an aerodynamic shape optimization methodology on three benchmark problems. The methodology is based on a Newton-Krylov-Schur flow solver for the Euler and RANS equations, a geometry parameterization based on B-spline surfaces, an efficient integrated mesh movement algorithm based on B-spline volumes, a discrete-adjoint gradient computation achieved with a complete hand linearization of the discrete flow and mesh residual equations, and a sequential quadratic programming algorithm for constrained minimization. The three cases investigated are:

1. Drag minimization of a symmetrical two-dimensional airfoil in transonic inviscid flow under the constraint that the airfoil have a thickness greater than or equal to that of the NACA 0012 airfoil at all chordwise positions.

2. Lift-constrained drag minimization through optimizing the twist distribution of a rectangular wing with NACA 0012 sections in subsonic inviscid flow.

3. Drag minimization through optimizing the section shapes and twist distribution of the CRM wing with a blunt trailing edge in transonic turbulent flow subject to lift and pitching moment constraints.

The first case is designed such that the shock waves cannot be completely eliminated. Nevertheless, the optimizer is able to weaken the shocks and move them aft such that the drag is reduced by 86% to roughly 60 drag counts. The second case, which was originally studied by Hicken and Zingg,[3] provides an opportunity to demonstrate that the optimization methodology can produce a known result, the elliptical spanwise lift distribution associated with minimum induced drag for a planar wake. The optimized geometry has a spanwise lift distribution very close to elliptical and a spanwise efficiency factor close to unity, as expected. The third case is in a turbulent flow and hence requires optimization based on the RANS equations. For this case, the optimization does not reduce the optimality measure as far as for the other two cases, but

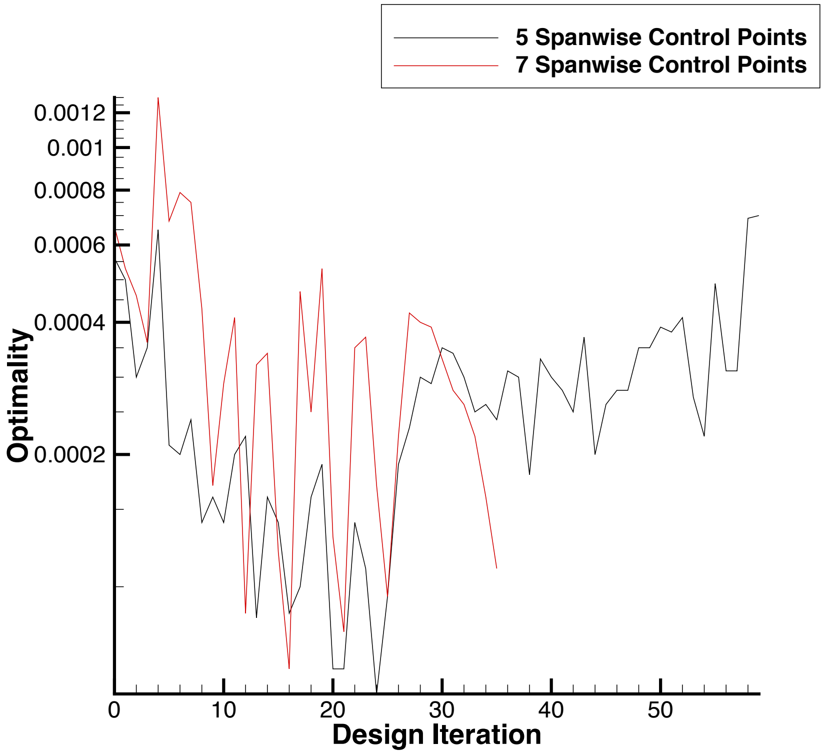

Figure 18. Optimization convergence history

a significant drag reduction of 11 counts or 6% is achieved by reducing both induced and wave drag. It is possible that deeper convergence can be obtained by adding geometric constraints near the leading and trailing edges and the wing tip.

These results demonstrate the overall effectiveness of the aerodynamic shape optimization methodology used in Jetstream, which is able to provide significant drag reductions in all three cases. The three optimization cases studied provide the opportunity to characterize and evaluate aerodynamic shape optimization methodologies. It is recommended that the suite be broadened to include test problems requiring larger geometric changes between the initial and final geometries, including, for example, planform changes, i.e. sweep and span, nonplanar geometries such as winglets, and wing-body-tail configurations. Moreover, these cases should focus on optimization based on the RANS equations, as Osusky and Zingg[2] have shown that wings optimized based on the Euler equations do not perform particularly well when analyzed in turbulent flow, both because shock waves can reappear and trailing edge separation can occur, even at cruise conditions.

References

[1]Osusky, L. and Zingg, D. W., "A Novel Aerodynamic Shape Optimization Approach for Three-Dimensional Turbulent Flows," *50th AIAA Aerospace Sciences Meeting*, AIAA–2012–0058, Nashville, Tennessee, United States, Jan. 2012.

[2]Osusky, L. and Zingg, D. W., "Application of an efficient Newton-Krylov algorithm for aerodynamic shape optimization based on the Reynolds-Averaged Navier-Stokes equations," *21st AIAA Computational Fluid Dynamics Conference*, AIAA–2013–2584, San Diego, California, United States, June 2013.

[3]Hicken, J. E. and Zingg, D. W., "Aerodynamic optimization algorithm with integrated geometry parameterization and mesh movement," *AIAA Journal*, Vol. 48, No. 2, Feb. 2010, pp. 400–413.

[4]Truong, A. H., Oldfield, C. A., and Zingg, D. W., "Mesh movement for a discrete-adjoint Newton-Krylov algorithm for aerodynamic optimization," *AIAA Journal*, Vol. 46, No. 7, July 2008, pp. 1695–1704.

[5]Meijerink, J. A. and van der Vorst, H. A., "An iterative solution method for linear systems of which the coefficient matrix is a symmetric M-matrix," *Mathematics of Computation*, Vol. 31, No. 137, Jan. 1977, pp. 148–162.

[6]Hicken, J. E. and Zingg, D. W., "A parallel Newton-Krylov solver for the Euler equations discretized using simultaneous approximation terms," *AIAA Journal*, Vol. 46, No. 11, Nov. 2008, pp. 2773–2786.

[7]Osusky, M., Hicken, J. E., and Zingg, D. W., "A parallel Newton-Krylov-Schur flow solver for the Navier-Stokes equations

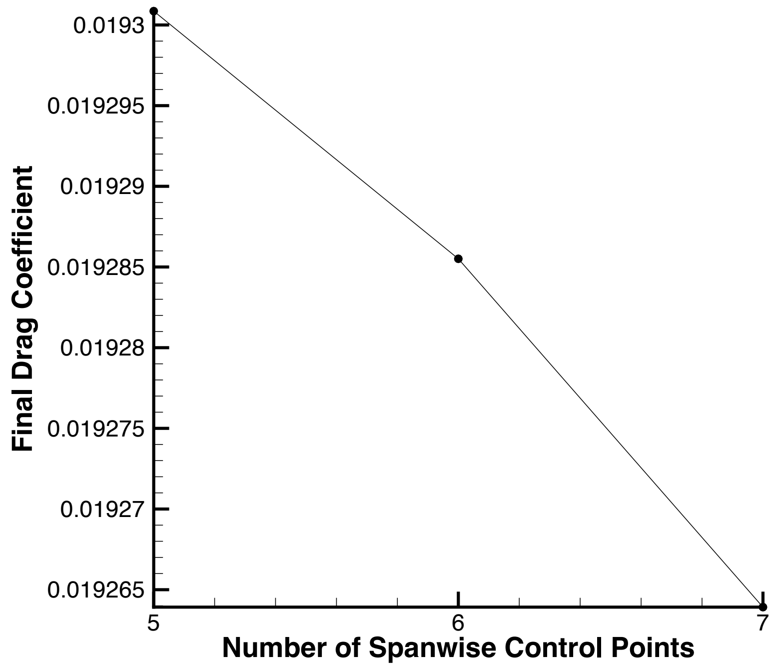

Figure 19. CRM drag results

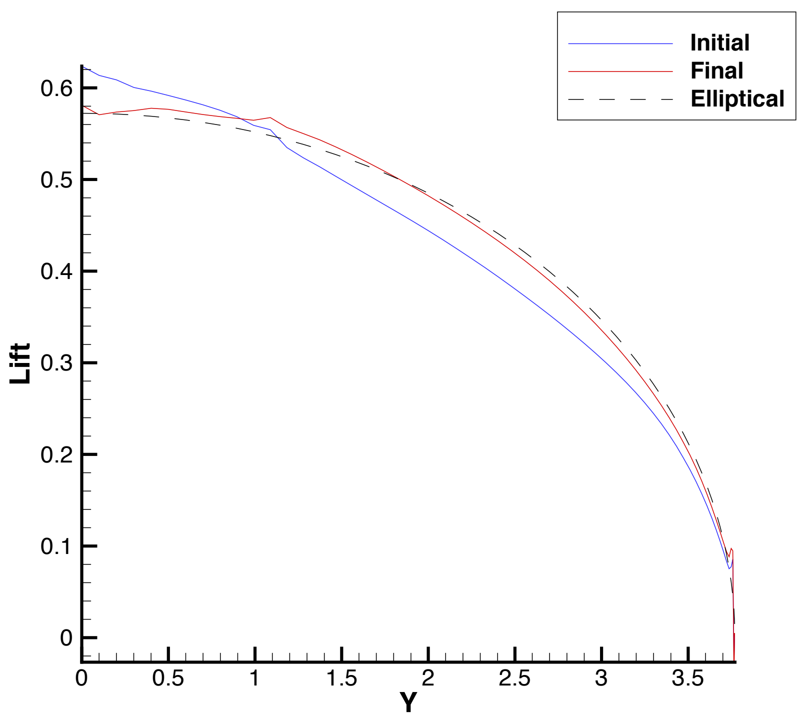

Figure 20. Spanwise lift distribution, 7 spanwise control points

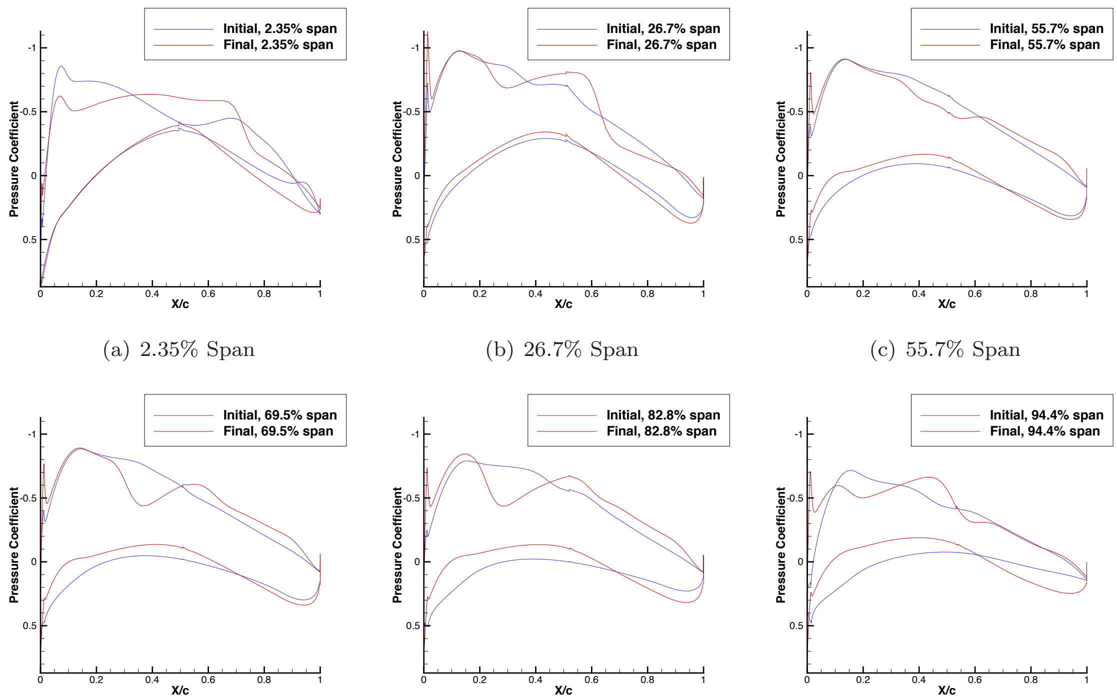

(a) 2.35% Span (b) 26.7% Span (c) 55.7% Span

(d) 69.5% Span (e) 82.8% Span (f) 94.4% Span

Figure 21. Comparison of initial and final surface pressure coefficient distributions, 7 spanwise control points

using the SBP-SAT approach," *48th AIAA Aerospace Sciences Meeting and Aerospace Exposition*, AIAA–2010–116, Orlando, Florida, United States, Jan. 2010.

[8]Gill, P. E., Murray, W., and Saunders, M. A., "SNOPT: an SQP algorithm for large-scale constrained optimization," *SIAM Journal on Optimization*, Vol. 12, No. 4, 2002, pp. 979–1006.

[9]Pironneau, O., *Optimal shape design for elliptic systems*, Springer-Verlag, 1983.

[10]Jameson, A., "Aerodynamic design via control theory," *Journal of Scientific Computing*, Vol. 3, No. 3, 1988, pp. 233–260.

[11]Hicken, J. E. and Zingg, D. W., "A Simplified and Flexible Variant of GCROT for Solving Nonsymmetric Linear Systems," *SIAM Journal on Scientific Computing*, Vol. 32, No. 3, 2010, pp. 1672–1694.

[12]Vassberg, J. C., Harrison, N. A., Roma., D. L., and Jameson, A., "A Systematic Study on the Impact of Dimensionality for a Two-Dimensional Aerodynamic Optimization Model Problem," *29th AIAA Applied Aerodynamics Conference*, Honolulu, Hawaii, June 2011, pp. 1–19.

[13]Hoschek, J., "Intrinsic parametrization for approximation," *Computer Aided Geometric Design*, Vol. 5, No. 1, 1988, pp. 27–31.

[14]Vassberg, J. C., Tinoco, E. N., Mani, M., Rider, B., Zickuhr, T., Levy, D. W., Brodersen, O. P., Eisfeld, B., Crippa, S., Wahls, R. A., Morrison, J. H., Mavriplis, D. J., and Murayama, M., "Summary of the Fourth AIAA CFD Drag Prediction Workshop," *28th AIAA Applied Aerodynamics Conference*, AIAA–2010–4547, Chicago, Illinois, United States, June 2010.

[15]Levy, D. W., Laflin, K. R., Tinoco, E. N., Vassberg, J. C., Mani, M., Rider, B., Rumsey, C. L., Wahls, R. A., Morrison, J. H., Brodersen, O. P., Crippa, S., Mavriplis, D. J., and Murayama, M., "Summary of Data from the Fifth AIAA CFD Drag Prediction Workshop," *51st AIAA Aerospace Sciences Meeting and Aerospace Exposition*, AIAA–2013–0046, Grapevine, Texas, United States, Jan. 2013.

[16]Buckley, H. P. and Zingg, D. W., "Approach to aerodynamic design through numerical optimization," *AIAA Journal*, Vol. 51, No. 8, in press,2013.

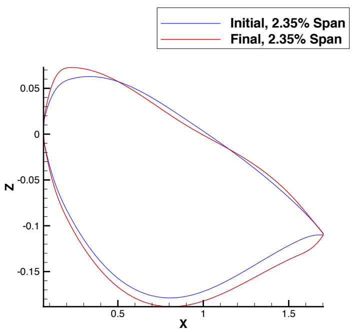

(a) 2.35% Span

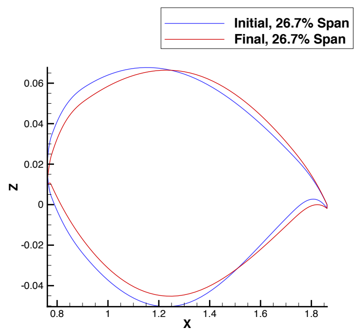

(b) 26.7% Span

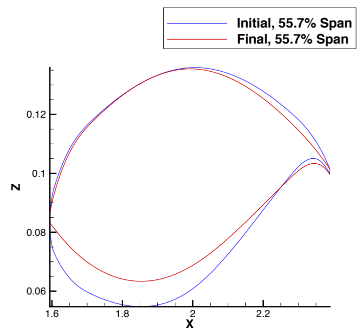

(c) 55.7% Span

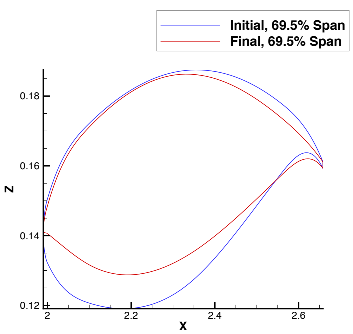

(d) 69.5% Span

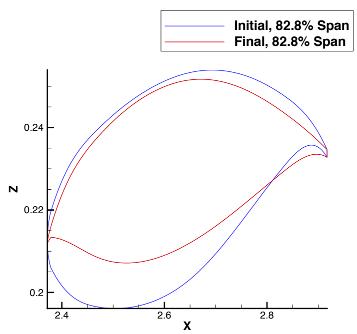

(e) 82.8% Span

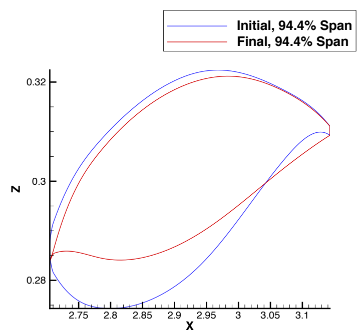

(f) 94.4% Span

Figure 22. Comparison of initial and final airfoil shapes, 7 spanwise control points